

# 1 Modeling tabular icebergs coupled to an ocean model

2 **A. A. Stern<sup>1</sup>, A. Adcroft<sup>1</sup>, O. Sergienko<sup>1</sup>, G. Marques<sup>1</sup>, R. Hallberg<sup>1</sup>**

3 <sup>1</sup>Geophysical Fluid Dynamics Laboratory, Princeton University

4 <sup>1</sup>201 Forrestal Rd, Princeton, NJ 08540, USA

## 5 **Key Points:**

- 6 • = enter point 1 here =  
7 • = enter point 2 here =  
8 • = enter point 3 here =

9      **Abstract**

10     The calving of large tabular icebergs from the Antarctic ice shelves accounts for approximately half of Antarctic ice-shelf decay. After calving, these tabular icebergs drift across  
 11    large distances, altering regional ocean circulation, bottom-water formation, sea-ice production  
 12    and biological primary productivity in the icebergs' vicinity. However, despite  
 13    their importance, the current generation of numerical models is unable to represent large  
 14    tabular icebergs in a physically realistic way. In this study we develop a novel framework  
 15    to model large tabular icebergs submerged in the ocean. In this framework, tabular ice-  
 16    bergs are constructed out of Lagrangian elements that drift in the ocean, and are held to-  
 17    gether by numerical bonds. By breaking these bonds, a tabular iceberg can be made to  
 18    split into smaller pieces, or to break away from an ice shelf. We describe the Lagrangian  
 19    bonded iceberg model and discuss a number of the technical elements involved in its de-  
 20    velopment. We demonstrate the capabilities of the model by modeling a tabular iceberg  
 21    drifting away an idealized ice shelf.

23      **1 Introduction**

24     The Antarctic ice shelves are characterized by large infrequent calving events where  
 25    massive pieces of the ice shelves break off, to create large tabular icebergs. Observational  
 26    estimates suggest that over the past 30 years approximately half of Antarctic ice-shelf de-  
 27    cay is due to iceberg calving, while the other half occurs through ice-shelf melting [De-  
 28    poorter et al , 2013; Rignot et al , 2013]. Iceberg sizes appear to fit a power law distri-  
 29    bution, with the majority of icebergs being small ( $L < 1$  km), while the far less numerous  
 30    large tabular icebergs ( $L > 5$  km) account for more than 90% of the icebergs mass [Tour-  
 31    nadre et al , 2016].

32     After calving, icebergs slowly drift away from their source glaciers, often becom-  
 33    ing stuck in sea ice, or grounding along the Antarctic coast [Lichey and Hellmer , 2001;  
 34    Dowdeswell and Bamber , 2007]. Large tabular icebergs extend deep into the water col-  
 35    umn, and have the potential to disrupt ocean circulation patterns for months or even years  
 36    after calving [Robinson et al , 2012; Stern et al , 2015]. The freshwater flux from iceberg  
 37    melt impacts ocean hydrography around the iceberg, influencing sea-ice production and  
 38    bottom-water formation [Arrigo et al , 2002; Robinson et al , 2012; Nicholls et al , 2009;  
 39    Fogwill et al , 2016]. The long distances traveled by large icebergs before melting means  
 40    that their meltwater impact is often felt hundreds of kilometers away from their calving  
 41    origins [Stern et al , 2016]. Meltwater injection (and the accompanying upwelling) from  
 42    icebergs can also influence biological productivity by providing nutrients to the surface  
 43    ocean or changing sea ice conditions [Arrigo et al , 2002; Vernet et al , 2012; Biddle et  
 44    al , 2015]. The increased productivity associated with free-floating tabular icebergs has  
 45    been linked with local increases in ocean carbon uptake, potentially large enough to be a  
 46    significant fraction of the Southern Ocean carbon sequestration [Smith et al , 2007].

47     In recent years, there has been an increased interest in iceberg drift and decay. This  
 48    surge of interest has been driven by (i) the need to understand polar freshwater cycles  
 49    in order to create realistic climate forecasts and sea level projections [Silva et al , 2006;  
 50    Shepherd and Wingham , 2007; Rignot et al , 2013]; and (ii) the increased use of high-  
 51    latitudes iceberg-filled waters for shipping lanes and offshore hydrocarbon exploration  
 52    in the Arctic [Pizzolato et al , 2012; Unger , 2014; Henderson and Loe , 2016]. The in-  
 53    creased interest in icebergs has led to the development of numerical models of iceberg  
 54    drift and decay [Mountain , 1980; Bigg et al , 1997; Gladstone et al , 2001; Kubat et al  
 55    , 2005], some of which have been included in global General Circulation Models [Mar-  
 56    tin and Adcroft , 2010; Marsh et al , 2015]. These iceberg drift models treat icebergs as  
 57    Lagrangian point particles, which are advected by the flow, and melt according to cer-  
 58    tain parameterizations for icebergs melt. Since icebergs are treated as point particles, ice-  
 59    berg drift models are mostly suitable for modeling icebergs smaller than an ocean grid

60 cell. Consequently, these models have mostly been used to represent icebergs smaller than  
 61 3.5 km on a global scale [Jongma et al , 2009; Martin and Adcroft , 2010; Marsh et al ,  
 62 2015].

63 Point-particle iceberg drift models are less suitable for modeling larger tabular ice-  
 64 bergs, where the size and structure of the iceberg may be an important feature in deter-  
 65 mining their drift and decay [Stern et al , 2016]. They also are not suitable for studying  
 66 the local effects that icebergs have on the surrounding ocean, or the small scale processes  
 67 that influence iceberg melt and decay [Wagner et al , 2014; Stern et al , 2015]. For this  
 68 reason, tabular icebergs ( $L > 5$  km) are currently not represented in the iceberg drift mod-  
 69 els used in climate models, even though observations suggest that tabular icebergs account  
 70 for the vast majority of the total Southern Hemisphere iceberg mass [Tournadre et al ,  
 71 2016].

72 The goal of this study is to develop a new iceberg model where tabular icebergs are  
 73 explicitly resolved. In this model, icebergs are no longer treated as point particles that in-  
 74 teract with the ocean at a single location, but rather icebergs are given structure, so that  
 75 they interact with the ocean across multiple ocean grid cells and depress the ocean surface  
 76 over a wide area. To do this, we create tabular icebergs out of many Lagrangian elements  
 77 with finite extent which are ‘bonded’ together by numerical bonds. The numerical bonds  
 78 hold the ice elements together and allow a collection of elements to move as a unit (see  
 79 schematic in Figure 1). By manually breaking these bonds, we can simulate iceberg calv-  
 80 ing, allowing us to study the ocean response to a large tabular iceberg detaching from an  
 81 ice shelf (e.g.: Figure 2 and 3) or the fracturing of a large iceberg into smaller pieces.

82 The Lagrangian model developed in this study is referred to at the Lagrangian Bonded  
 83 Iceberg Model (LBIM). Section 2 gives a description of many of the key aspects of the  
 84 LBIM. Since this model is a new approach to modeling icebergs, we present many of the  
 85 technical elements involved in constructing the model. In section 3 and 4, we demonstrate  
 86 the capabilities of the model by simulating a tabular iceberg detaching from an idealized  
 87 ice shelf.

## 88 2 Model description

89 The LBIM is a Lagrangian particle-based model (or discrete element model) in that  
 90 the objects of the model are Lagrangian elements. Each element represents a mass of ice  
 91 that is floating in the ocean, and has a position, velocity, mass, and a set of dimensions,  
 92 which can evolve in time. The motion of each element is determined by a momentum  
 93 equation which is solved in the (Lagrangian) reference frame of the element. The ele-  
 94 ments are forced by oceanic and atmospheric forces, which are provided by the user, or  
 95 are determined by coupling the LBIM to an ocean/atmosphere model. The elements also  
 96 interact with one another and can be bonded together to form larger structures. The an-  
 97 gular momentum of the elements is not modeled explicitly; instead rotational motion of  
 98 larger structures emerge as a consequence of bond orientation and collective motion. In  
 99 different contexts, the LBIM elements can be thought to represent individual icebergs, sea  
 100 ice flows, or, when the elements are bonded together, they can represent larger structures  
 101 such as tabular icebergs or ice shelves.

102 The LBIM is developed on the code base of an existing iceberg drift model [Martin  
 103 and Adcroft , 2010; Stern et al , 2016]. When run with the correct set of runtime flags,  
 104 the model runs as a traditional iceberg drift model.

### 105 2.1 Equations of motion

106 The elements drift in the ocean, forced by atmosphere, ocean and sea-ice drag forces,  
 107 as well as the Coriolis force and a force due to the sea surface slope. When these ice el-

ements move alone (without interactions with other elements), they can be thought of as representing individual (or clusters of) small icebergs, and follow the same equations described in the iceberg drift model of Martin and Adcroft [2010] (based on the equations outlined in Bigg et al [1997] and Gladstone et al [2001]).

In addition to the environmental forces, the elements in the LBIM experience interactive forces due to the presence of other elements. Two types of interactive forces are included between elements. The first force is a repulsive force which is applied to elements to prevent them from moving too close to one another. This repulsive force prevents icebergs from piling up on top of one another. The second interactive force is a force due to numerical ‘bonds’, and is only applied if two elements are labelled as ‘bonded’. When two elements are bonded, each element feels an attractive force that prevents the elements from moving too far apart from one another. The interactive forces between two bonded elements are defined such that in the absence of other forces the elements come to rest adjacent to one another, with no overlap of the iceberg areas.

The momentum equation for each element is given by

$$M \frac{D\vec{u}}{Dt} = \vec{F}_A + \vec{F}_W + \vec{F}_R + \vec{F}_C + \vec{F}_{SS} + \vec{F}_{SI} + \vec{F}_{IA}, \quad (1)$$

where  $\frac{D}{Dt}$  is the total (Lagrangian) derivative,  $M$  is the mass of the element,  $\vec{u}$  is the velocity of the element, and the terms on the right hand side give the forces on the element due to air drag ( $\vec{F}_A$ ), water drag ( $\vec{F}_W$ ), sea ice drag ( $\vec{F}_{SI}$ ), Coriolis force ( $\vec{F}_C$ ), wave radiation force ( $\vec{F}_R$ ), sea surface slope ( $\vec{F}_{SS}$ ), and interactions with other elements ( $\vec{F}_{IA}$ ). The environmental forces are the same as those presented in Martin and Adcroft [2010], and are provided for completeness in Appendix A. The details of the interactive forces are provided in below.

## 2.2 Interactive Forces

The interactive force on an element is calculated by adding together the interactions with all other elements, such that the interactive force on element  $i$ ,  $(\vec{F}_{IA})_i$  is given by:

$$(\vec{F}_{IA})_i = \sum_{j \neq i} (\vec{F}_{IA})_{ij}, \quad (2)$$

where  $(\vec{F}_{IA})_{ij}$  is the force on element  $i$  by element  $j$ . Both bonded and repulsive interactions are modeled using elastic stresses with frictional damping. The elastic component of the force is a function of the distance between the two elements, while the frictional damping force depends on the relative velocity of the two elements.

To describe the forces between two elements, we begin by introducing some notation. Let  $\vec{x}_i$ ,  $\vec{x}_j$  be the positions of elements  $i$  and  $j$ . The distance between elements  $i$  and  $j$  is

$$d_{ij} = |\vec{x}_i - \vec{x}_j|. \quad (3)$$

When calculating the interactive forces between elements, the elements are assumed to be circular. We define the interaction diameter of an element by

$$D_i = 2 \sqrt{\frac{A_i}{\pi}}, \quad (4)$$

where  $A_i$  is the planar surface area of element  $i$ . Using this, we define the critical interactive length scale,

$$L_{ij} = \frac{D_i + D_j}{2}, \quad (5)$$

which governs interactions between elements  $i$  and  $j$ . Repulsive forces are only applied when  $d_{i,j} < L_{i,j}$ , while for  $d_{i,j} > L_{i,j}$  attractive bonded forces are applied when a bond exists between element  $i$  and  $j$ . Bond and repulsive forces are designed such that in the

absence of other forces, bonded particles will settle in an equilibrium position where elements are separated by the critical interaction length scale  $L_{i,j}$ .

To aid in notation, we define a bond matrix  $B_{ij}$  such that  $B_{ij} = 1$  if elements i and j are bonded together and  $B_{ij} = 0$  otherwise. Using this notation, the interactive force  $(\vec{F}_{IA})_{ij}$  on an element i by an element j is given by

$$(\vec{F}_{IA})_{ij} = \begin{cases} (\vec{F}_e)_{ij} + (\vec{F}_d)_{ij} & \text{if } d_{ij} \leq L_{ij} \\ (\vec{F}_e)_{ij} + (\vec{F}_d)_{ij} & \text{if } d_{ij} > L_{ij} \text{ and } B_{ij} = 1 \\ 0 & \text{if } d_{ij} > L_{ij} \text{ and } B_{ij} = 0 \end{cases} \quad (6)$$

$(\vec{F}_e)_{ij}$  and  $(\vec{F}_d)_{ij}$  are the elastic and frictional damping components of the interactive force between elements i and j. The elastic force  $(\vec{F}_e)_{ij}$  between elements is given by

$$(\vec{F}_e)_{ij} = -\kappa_e (d_{i,j} - L_{i,j}) T_{i,j} \vec{r}_{ij}, \quad (7)$$

where  $\vec{r}_{ij} = \frac{(\vec{x}_i - \vec{x}_j)}{|\vec{x}_i - \vec{x}_j|}$  is the directional unit vector between the position of element i and j,  $\kappa_e$  is the spring constant, and  $T_{i,j}$  is the minimum of the thickness of elements i, j. The interactive forces obey Newton's 3rd Law (i.e.:  $(\vec{F}_{IA})_{ij} = -(\vec{F}_{IA})_{ji}$ ). The minimum thickness,  $T_{i,j}$ , is preferred to the average thickness, since this means that for two bonded elements a fixed distance apart, the acceleration due to elastic forces is bounded, even when the thickness of one of the elements approaches zero.

The frictional damping force has components that damp both the relative radial velocity and relative transverse velocities of the two elements. If  $\vec{r}_{ij}^\perp$  is the direction vector perpendicular to  $\vec{r}_{ij}$ , and  $P_{\vec{r}_{ij}}$  and  $P_{\vec{r}_{ij}^\perp}$  are the projection matrices that project onto  $\vec{r}_{ij}$  and  $\vec{r}_{ij}^\perp$  respectively, then the frictional damping force is given by

$$(\vec{F}_d)_{ij} = \left( -c_r P_{\vec{r}_{ij}} - c_t P_{\vec{r}_{ij}^\perp} \right) \cdot (\vec{u}_i - \vec{u}_j) \quad (8)$$

Here  $c_r$  and  $c_t$  are the radial and transverse drag coefficients. For the simulation below, we set  $c_r = 2\sqrt{\kappa_e}$  and  $c_t = \frac{1}{4}c_r$  so that the radial elastic force is critically damped, and the transverse damping is sub critical. The damping forces are implemented using an implicit time stepping scheme, to avoid stability issues for very small elements (details found in Appendix B).

The effectiveness of the repulsive forces can be seen in Figure 4, which shows an uncoupled (ice only) simulation where ice elements drift westward into a bay, and eventually come to rest with minimal overlap between elements. The effectiveness of the numerical bonds is demonstrated in Figure 5, where tabular icebergs (constructed from many ice elements bonded together) and individual icebergs (unbonded elements) drift together towards a convex coast line. When the tabular icebergs arrive at the coast, they bump into the coastline and begin to rotate, influencing the paths of the other icebergs. In this example we see that modeling large structures using small elements bonded together, allows us to achieve large-scale structure and rotational motion, without having to include an equation for the angular momentum of the elements (as discussed in Jakobsen [2001]). Animations of these uncoupled simulations can be found in the supplementary materials.

### 2.3 Initializing element geometry and packing

For purposes of packing, we assume that elements have surface areas which are shaped as equally-sized regular hexagons (note that the elements are assumed to be circular for purposes of interactions, but are assumed to be hexagonal for packing purposes). When packing these elements together, the hexagonal elements are initially arranged in a staggered lattice, with each element bonded to the adjacent elements (see Figure 1). In this arrangement, each element (away from the edges) is bonded to six other elements.

187 The bonds between elements form a pattern of equilateral triangles, which give the larger  
 188 structure rigidity. The circular shape of elements (used for interactions) is inscribed within  
 189 the hexagonal shape used for packing (Figure 1). The centers of adjacent elements are ini-  
 190 tially separated by a distance  $d_{i,j} = L_{i,j} = 2A_p$ , where  $A_p$  is the length the apothems of  
 191 the hexagons.

192 Some experiments were also performed using rectangular elements, arranged in a a  
 193 regular (non-staggered) lattice. In this case, each element forms four bonds with adjacent  
 194 elements. However, the resultant structures were found to be much less rigid and tended  
 195 to collapse when sufficient forces was applied. For this reason, hexagonal elements are  
 196 used here.

## 197 2.4 Ocean-ice and ice-ocean coupling

198 The LBIM is coupled to the ocean model via a two-way synchronous coupling,  
 199 meaning that ocean-model fields are passed to the LBIM, and the LBIM fields are passed  
 200 back to the ocean model at every time step. Passing fields between the two models in-  
 201 volves interpolating the fields from the ocean model's Eulerian grid onto the LBIM's 'La-  
 202 grangian grid' (i.e.: onto the ice elements, Figure 1), and aggregating fields from the La-  
 203 grangian elements onto the ocean-model's Eulerian grid.

204 The coupling from the ocean model to the LBIM is straight forward: at every time  
 205 step, the ocean mixed layer temperature, salinity, velocity and sea-ice concentration are  
 206 passed from the ocean model to the LBIM, to be used in the momentum and thermo-  
 207 dynamic equations of the ice elements. Since tabular icebergs are explicitly resolved in  
 208 the ocean, it is sufficient for each element to interact with ocean mixed layer only (i.e.:  
 209 there is no need to manually embed icebergs into the ocean by integrating ocean fields  
 210 over the icebergs' thickness, as suggested in Merino et al [2016]). Within the LBIM, the  
 211 ocean model fields are interpolated onto the Lagrangian grid using a bilinear interpolation  
 212 scheme. The LBIM is not sensitive to the chosen interpolation scheme.

213 The coupling from the LBIM to ocean model is more complex. The LBIM influ-  
 214 ences the ocean by: (i) applying a pressure to the ocean surface, (ii) imposing heat, salt  
 215 and mass fluxes on the ocean, associated with ice melting, and (iii) affecting the upper  
 216 ocean by applying a no-slip boundary condition and frictional velocity beneath the ice.  
 217 Fields from the LBIM are aggregated from the Lagrangian elements to the Eulerian ocean  
 218 grid before they are passed to the ocean model. Since LBIM applies large pressures to  
 219 the ocean surface, the ocean model is sensitive to the aggregation scheme used to map the  
 220 LBIM fields to the ocean grid. Sudden jumps to the ocean surface pressure can trigger  
 221 tsunamis within the ocean model, making the ocean model unrealistic.

222 The aggregation of the LBIM fields onto the ocean grid is done in a way that is  
 223 consistent with the shape of the elements in the LBIM (see Section 2.3). Fields are 'spread'  
 224 to the ocean model grid by exactly calculating what fraction of an element's surface area  
 225 lies in a particular grid box, and dividing the field in proportion to this fraction. For ex-  
 226 ample, consider a hexagonal element in the LBIM, which is positioned such that it inter-  
 227 sects four ocean grid cells (inset panel in Figure 1). In this situation, the mass of the ele-  
 228 ment is divided between these four ocean cells in proportion to the overlap area between  
 229 the hexagonal element and the grid cell (this fraction is shown by the colors in the inset  
 230 panel in Figure 1). An advantage of this approach is that there are no jumps in pressure as  
 231 an element moves from one grid cell to another.

232 The numerical calculation of the intersection between hexagons and the ocean grid  
 233 is simplified by dividing the hexagon into 6 equilateral triangles. This method allows for  
 234 the intersection to be found even when the hexagon is not aligned with the grid.

235 The aggregation scheme is coded with the restriction that an element's area can only  
 236 intersect a maximum of four ocean grid cells at a time. A consequence of this is that this  
 237 sets a limit on the maximum size of elements that can be represented using this model,  
 238 i.e.: the longest horizontal dimension of an ice element must be smaller than the ocean  
 239 grid spacing. Larger ice structures are constructed by bonding together smaller elements.

## 240 2.5 Thermodynamics

241 The ice elements decay according to a number of melt parameterizations. As the  
 242 ice elements melt, their mass decreases, and the appropriate salt, mass and heat fluxes are  
 243 passed to the ocean. In this section we described the melt parametrization for bonded,  
 244 unbonded and partially bonded elements.

245 As mentioned above, ice elements which do not interact with other elements are  
 246 modeled identically to the point particle icebergs described in Martin and Adcroft [2010].  
 247 These elements melt according to three semi-empirical parametrization for melt commonly  
 248 used in previous iceberg studies [Gladstone et al , 2001; Martin and Adcroft , 2010].  
 249 Three types of iceberg melting are used: basal melt,  $M_b$ , melt due to wave erosion,  $M_e$   
 250 and melt due to buoyant convection,  $M_v$ .  $M_e$  and  $M_v$  are applied to the sides of the ice  
 251 element, while  $M_b$  is applied at the ice element base. The details of  $M_b$ .  $M_v$  and  $M_e$  are  
 252 given in Appendix A.

253 When multiple elements are bonded together to form larger structures, it is no longer  
 254 appropriate to use the parameterizations for melt developed for individual point-particle  
 255 icebergs. An element which is completely surrounded by other elements, is meant to rep-  
 256 resent a piece of ice in the middle of a large structure, and hence will not experience a  
 257 melt at its sides due to wave erosion or buoyant convection. Also, the iceberg basal melt  
 258 rate,  $M_b$  described above is based on boundary layer theory of flow past a finite plate, and  
 259 is only appropriate for basal surfaces where the distance from the leading edge is suffi-  
 260 ciently small [Eckert , 1950; Weeks and Campbell , 1973]. For an element in the interior  
 261 of large structures, the distance from the edge of the structure is large, and so using  $M_b$   
 262 for the basal melt is not appropriate. Instead, the basal melt,  $M_s$  is determined using the  
 263 three equation model for basal melt, which is a typical melting parametrization beneath  
 264 used beneath ice shelves [Holland and Jenkins , 1999].

265 When using both individual elements and bonded elements in the same simulation,  
 266 we determine which melt rate parameterizations to use based on the amount of bonds  
 267 that each element has. An element which is in the center of a large structure will form  
 268 the maximum number of bonds, while unbonded elements form zero bonds. If maximum  
 269 number of bonds that an element can form (given the shape of the element) is  $N_{max}$ , and  
 270 the number bonds that an element has is  $N_b$ , then the side melt and bottom melt for that  
 271 element are given by

$$M_{side} = \frac{(N_{max} - N_b)}{N_{max}} (M_v + M_e) \quad (9)$$

272 and

$$M_{bottom} = \frac{(N_{max} - N_b)}{N_{max}} M_b + \frac{N_b}{N_{max}} M_s \quad (10)$$

273 respectively. In this way, elements with no bonds, melt like point-particle icebergs, ele-  
 274 ments at the center of large structures melt like ice shelves, and elements at the sides of  
 275 large structures have a combination of iceberg side and basal melt, and ice-shelf melt.

## 276 2.6 Algorithms and computational efficiency

277 Including interactions between elements leads to an increase in the computational  
 278 complexity of the model. In this subsection we comment on some of the algorithmic pro-  
 279 cedures that have been used to increase the computational efficiency.

280      **2.6.1 Interactions and Bonds**

281      At every time step, we calculate the force on each element due to interactions with  
 282      every other element. In principle, this involves order  $N^2$  operations (for N elements).  
 283      However, since each element only has repulsive interactions with elements that are less  
 284      than one ocean grid cell away, and each element only has bonded interactions with a  
 285      small number of other elements, we are able to reduce the complexity of the system.

286      The complexity reduction is achieved by storing the element data in an efficient way  
 287      that prevents having to search through all element pairs to check if they are close to one  
 288      another or are bonded with one another. The data storage system works as follows: point-  
 289      ers to the memory structures containing each element are stored in linked list data struc-  
 290      tures, which allow elements to be added and removed from the lists easily without re-  
 291      structuring the entire list. Instead of using one list for all the elements on a processor (as  
 292      was done in the original code [Martin and Adcroft , 2010]), we use a separate linked list  
 293      for each ocean grid cell. When an element moves between ocean grid cells, it is removed  
 294      from its original list and added to the list corresponding to its new ocean grid cell. Since  
 295      the area of elements has to be smaller than the area of an ocean grid cell, the critical in-  
 296      teraction length scale (equation 5) is less than the length of a grid cell. This means that  
 297      elements only experience repulsive forces with elements in the same ocean grid cell, or  
 298      in one of the 8 adjacent cells. Limiting the possible repulsive interactions to elements in  
 299      these 9 linked lists substantially reduces the computational time needed to calculate the  
 300      total interactive force.

301      Bonded interactions are handled differently. Each bond is assigned a piece of mem-  
 302      ory. Each ice element contains a linked list of each of its bonds (typically up to six bonds  
 303      per element). At each time step, the code traverses the lists of bonded elements, and adds  
 304      a bonded force corresponding to these bond. The bonded force is only applied if  $d_{i,j} >$   
 305       $L_{ij}$ , to avoid double counting an interaction. Having a list of bonds stored with each ele-  
 306      ment reduces the computational complexity of bonded interactions from order  $N^2$  to order  
 307      N. Handling bonded attractive forces separately to the repulsive and non-bonded forces  
 308      means that we do not need to check whether two elements are bonded, which further in-  
 309      creases the computational efficiency.

310      **2.6.2 Parallelization and halos**

311      The LBIM runs on multiple processors in parallel (and the same grid as the ocean  
 312      decomposition). When elements move from an ocean cell on one processor to an ocean  
 313      cell on a second processor, the memory has to be passed from one processor the next,  
 314      added and removed to the appropriate lists and the memory has to be allocated and deal-  
 315      located correctly. Element interactions across the edge of processors are handled using  
 316      computational halos. A computational halo is a copy of the edge of a one processor which  
 317      is appended to the edge of a second processor, so that the first processor can ‘see’ the sec-  
 318      ond processor during a time step. Before each time step, elements at the edges of each  
 319      processor are copied onto the halos of adjacent processors so that they can be used in cal-  
 320      culating the interactive forces. After each time step, these halos are removed, and the pro-  
 321      cess is repeated. These halo updates are one of the most computationally expensive parts  
 322      of the LBIM.

323      Keeping track of pairs of bonded elements that move across a processor edge re-  
 324      quires a lot of book keeping since bonds have to be severed and reconnected. Details of  
 325      how the bonds are broken and reconnected across processor boundaries are provided in  
 326      Appendix C.

327      **2.6.3 Time stepping**

328      The ice elements in the LBIM are advected using a semi-implicit velocity Verlet  
 329      time-stepping scheme. The velocity Verlet time stepping scheme is commonly used in  
 330      DEM models in video games because it is computational efficient and has desirable stabil-  
 331      ity properties [Jakobsen , 2001]. This time stepping scheme was preferred to the Runge-  
 332      Kutta 4, which was used in the iceberg model of Martin and Adcroft [2010] since the  
 333      Verlet time stepping only requires a calculation of the interactive forces once per time step  
 334      (while the Runge-Kutta scheme requires the interactive forces to be calculated four times).  
 335      Since the calculation of the interactive forces is one of the most computationally expen-  
 336      sive part of the algorithm, the Verlet scheme leads to a significant increase in the speed of  
 337      the model. We note that the Verlet scheme used in the LBIM contains a modification of  
 338      the original (fully explicit) velocity Verlet time stepping scheme in that damping terms are  
 339      treated implicitly (which increases the numerical stability). The details of this time step-  
 340      ping scheme are outlined in Appendix B.

341      **3 Experiment Setup**

342      The introduction of Lagrangian elements, numerical bonds and interpolation schemes  
 343      between the Eulerian and Lagrangian grids (discussed in Section 2) means that we now  
 344      have the tools to model large tabular icebergs submerged in the ocean. We demonstrate  
 345      this capability by simulating a tabular iceberg drifting away from an idealized ice shelf.

346      **3.1 Model configuration**

347      We initialized our simulation using the experimental setup created for the Marine  
 348      Ice Ocean Modeling Inter-comparison Project (MISOMIP) [Asay-Davis et al , 2016]. The  
 349      configuration consists of an idealized ice shelf in a rectangular domain. The domain is  
 350       $L_x = 80$  km wide and  $L_y = 480$  km long, and contains an ice shelf which is grounded on  
 351      the south side of the domain and has an ice front at  $y=650$  km. The ice thickness and  
 352      bottom topography of this setup are shown in Figure 6a and 6b respectively, with the  
 353      grounding line position drawn in for reference. The configuration is the same as that of  
 354      the Ocean0 setup in the MISOMIP, with a few minor changes to the ice-shelf geometry  
 355      (see Supplementary Material for details).

356      **3.2 Initializing Lagrangian elements:**

357      The idealized ice shelf is constructed out of Lagrangian ice elements. Ice elements  
 358      are hexagonal and are arranged in a regular staggered lattice (as discussed in Section 2.3).  
 359      The sides of the gridded hexagons are initialized with length  $S = 0.98$  km. Gaps along  
 360      the boundaries are filled in using smaller elements so that the total ice-shelf area is pre-  
 361      served. The initial mass of the ice elements is determined by a preprocessing inversion  
 362      step, which is the inverse of the ‘mass-spreading’ interpolation procedure discussed in  
 363      Section 2.3. The pre-interpolation ice draft (treating elements as point masses) contains  
 364      large grid artifacts (Figures 6c). These grid artifacts are much reduced after the mass-  
 365      spreading interpolation is applied (Figure 6b).

366      **3.3 Ocean model setup**

367      The LBIM is coupled to the MOM6 ocean model [Hallberg et al , 2013]. The ocean  
 368      model is run using a vertical coordinate system which is a hybrid between a sigma-level  
 369      and a z-level coordinate. In particular, model layers bend underneath the ice shelf as they  
 370      would in a sigma-coordinate model, but collapse to zero thickness when they intersect  
 371      with bottom topography, as they would in a z-level model. The coordinate system was  
 372      achieved using ALE regridding-remapping scheme [White et al , 2009]. The model uses a

373 horizontal resolution of 2 km, and 72 vertical layers. All simulations were repeated using  
 374 the ocean model configured in isopycnal mode (results were similar and are not presented  
 375 here).

376 Ocean parameters are as specified in the MISOMIP configuration [Asay-Davis et  
 377 al , 2016], and are shown in Table 1. The simulation is initially at rest, with horizontally  
 378 uniform initial ocean temperature and salinity profiles which vary linearly between spec-  
 379 ified surface and bottom values:  $T_{top} = -1.9^\circ \text{C}$ ,  $T_{bottom} = 1.0^\circ \text{C}$ ,  $S_{top} = 33.8 \text{ psu}$ ,  
 380  $S_{bottom} = 34.7 \text{ psu}$ . The maximum ocean depth is  $H_{ocean} = 720 \text{ m}$ . A sponge layer is  
 381 used on the northern boundary, which relaxes back to the initial temperature and salinity  
 382 with a relaxation time scale of  $T_{sponge} = 0.1 \text{ days}$ . Melting is set to zero for ocean cells  
 383 where the ocean column thickness is less than 10m to avoid using more energy to melt ice  
 384 than is present in the water column.

### 385 3.4 Spinup and iceberg calving:

386 The model is spun up for 5 years with all ice elements being held stationary. After  
 387 spinup, a large tabular iceberg is ‘broken off’ from the ice shelf, and allowed to drift into  
 388 the open ocean. This is achieved by allowing all ice elements initially within a 14.4 km  
 389 radius of the center of the ice front to move freely while the other ice elements continue  
 390 to be held stationary. Ice elements less than 12 km from the center of the ice front, are  
 391 bonded together to form a semi-circular tabular iceberg. A ring of elements whose dis-  
 392 tance,  $d$ , from the ice front center obeys  $12 \text{ km} \leq d \leq 14.4 \text{ km}$ , are allowed to move  
 393 freely, but have all their bonds removed. Elements in this half annulus represent fragments  
 394 of the ice shelf which calve into small pieces during a large calving event. Breaking the  
 395 bonds of these surrounding elements allows the tabular iceberg to move away from the  
 396 ice-shelf cavity more easily.

397 After the spinup period, a wind stress  $\vec{\tau} = < \tau_x, \tau_y > = < 0.05, 0.05 > \frac{N}{m^2}$  is applied  
 398 to drive the tabular iceberg away from the ice-shelf cavity. Perturbation experiments were  
 399 performed using other wind stress values.

## 400 4 Model Results

401 During spinup, the injection of buoyant meltwater at the base of the ice shelf drives  
 402 a clockwise circulation within the domain (not shown). The circulation compares well  
 403 with an identical static ice-shelf experiment run using an Eulerian ice shelf model [Gold-  
 404 berg et al , 2012] (a detailed comparison of the Lagrangian and Eulerian ice shelf models  
 405 is presented in a separate study, and is not shown here).

406 Once spinup is complete, the elements near the ice-shelf front are allowed to move  
 407 freely, and the icebergs begin to drift away from the ice shelf (see animations in the sup-  
 408 plementary materials). The semi-circular tabular iceberg moves as a cohesive unit due  
 409 to the presence of the numerical bonds, while the smaller ice fragments quickly disperse  
 410 (Figure 2). The tabular iceberg drifts towards the northward east, driven by the wind and  
 411 steered by the Coriolis force.

412 A warming of the surface waters is observed around the tabular iceberg, with the  
 413 largest warming occurring at the ice-shelf front and along the tabular iceberg’s rounded  
 414 edge (Figure 3). This surface warming is caused by upwelling of the warmer waters from  
 415 beneath the ice shelf and iceberg. As the icebergs drifts away from the ice shelf, these  
 416 warmer waters remain at the surface, mapping of the wake of the iceberg (Figure 3). The  
 417 signature of upwelling water in the wake of a drifting tabular iceberg bears some simi-  
 418 larity to satellite observations of streaks of increased ocean color in the wake of tabular  
 419 iceberg in the Southern Ocean [Duprat et al , 2016], suggesting that the increased pro-

420 ductivity around icebergs may be driven by upwelling water delivering nutrients to the  
421 surface.

422 The motion of the tabular iceberg disturbs the ocean surface, which drives ocean  
423 velocities through out the water column (Figure 7). The elevated shears around the tabu-  
424 lar iceberg lead to increased vertical mixing in the vicinity of the iceberg, which alters  
425 the stratification of the water column (Figure 8), heating the upper ocean. The increased  
426 ocean velocities and increased surface temperatures cause elevated melt rates at the base  
427 of the ice shelf and iceberg (Figure 9). The largest melt rates are observed at the newly  
428 calved ice-shelf front and on the rounded side of the iceberg (Figure 9a), where the ice-  
429 berg calving has created steep ice cliffs. These sharp ice fronts allow for large ocean  
430 currents (Figure 9c), which drive the elevated melt rates. The elevated melt rates act to  
431 smooth out the ice front over time, making the ice cliff less steep. While this is likely a  
432 real phenomena that could be observed in nature, we should be wary of the modeled ve-  
433 locities at the ice cliffs, since large changes in ice thicknesses are often associated with  
434 numerical pressure gradient errors which can drive spurious motion.

435 As mentioned above, the direction (and speed) of the iceberg drift is largely deter-  
436 mined by the wind speed and direction. Perturbation experiments using different wind  
437 stresses show that for sufficiently large winds, the tabular iceberg drifts to the north east  
438 when  $\tau_x > 0$ , and to the north west when  $\tau_x < 0$  (not shown). For a purely zonal wind  
439 stress with  $|\tau_x| \leq 0.01 \frac{N}{m^2}$ , the iceberg does not move away from the ice shelf. When the  
440 wind is purely offshore ( $\tau_x = 0.0 \frac{N}{m^2}$ ), a meridional wind stress  $\tau_y \geq 0.05 \frac{N}{m^2}$  is needed  
441 to move the tabular iceberg away from the ice shelf. While this result is partly an artifact  
442 of the artificial shape of the calving iceberg, it is also consistent with Bassis and Jacobs  
443 [2013] who noted that calving is a two step process consisting of (i) ice-shelf breaking  
444 and (ii) iceberg detachment. The results here suggest that strong (cross-shore) winds may  
445 be required to drive large tabular icebergs away from their mother glaciers.

446 Finally, we note that the numerical bonds in the LBIM are needed in order to allow  
447 the tabular iceberg to retain its shape. Comparing the iceberg calving simulation with an  
448 identical simulation where all numerical bonds have been removed, shows that in the ab-  
449 sence of the bonds, the ice elements quickly disperse (Figure 10). In this case, the model  
450 behavior is more similar to an ice-shelf disintegration and does not create a cohesive tabu-  
451 lar iceberg. By breaking some (but not all) numerical bonds, we can simulate the frac-  
452 turing of tabular icebergs, allowing tabular icebergs to break into smaller pieces (Figure  
453 ???). The breaking of a tabular iceberg increases decay rate of the iceberg by increasing  
454 the surface area of ice exposed to the ocean. Splitting the tabular iceberg into smaller  
455 fragments also allows the fragments of the iceberg to move more rapidly, and be more  
456 strongly influenced by the wind.

## 457 5 Summary

458 In this study we present a novel framework for representing tabular icebergs in nu-  
459 matical ocean models. In this framework, large tabular icebergs are constructed from col-  
460 lections of Lagrangian elements that are held together by numerical bonds. Constructing  
461 tabular icebergs out of many independent elements allows the icebergs to interact with  
462 the ocean across a wide area (larger than a grid cell), and behave as if they had a finite  
463 size and structure. This is in contrast to previous representations of icebergs in numerical  
464 models [Jongma et al , 2009; Martin and Adcroft , 2010; Marsh et al , 2015] that repre-  
465 sent icebergs as point particles. Explicitly resolving tabular icebergs in the ocean allows  
466 the icebergs to interact with the ocean in a more realistic way, and allows us to study the  
467 effect that tabular icebergs have on the ocean circulation. Including numerical bonds be-  
468 tween elements allows for the possibility of breaking bonds to simulation iceberg calving  
469 and fracture.

The capabilities of the tabular iceberg model were demonstrated by modeling a tabular iceberg drifting away from an idealized ice shelf (also constructed using Lagrangian elements). The results show that explicitly resolving the iceberg in the ocean allowed for a complex interaction between the tabular iceberg and the surrounding ocean. In our setup, the tabular iceberg is driven away from the ice shelf by ocean currents, wind stress, and the Coriolis force. As the iceberg moves through the water, it disturbs the ocean surface, driving barotropic ocean currents. The motion of the iceberg and melt beneath the iceberg drive upwelling along the sides of the iceberg, which entrains ambient water and causes a warming of the surface ocean in the wake of the iceberg. The changing ocean conditions feed back onto the iceberg, affecting its motion and melt rates. The highest melt rates are observed at edge of the iceberg which has the steepest ice cliff. These have the effect of smoothing out the ice edge over time. Simulations without using numerical bonds showed that these bonds are essential for allowing the iceberg to move as a unit. We also demonstrate that by breaking these numerical bonds we can simulate iceberg fracture, which is important process that increases the rate of iceberg decay.

To our knowledge, the model presented in this study is the first model to explicitly resolve drifting tabular icebergs in an ocean model that can be used for climate. A natural extension of this work is to try to include tabular icebergs into a general circulation model (GCM) used for climate projections. However, before this can be done, there are a number of issues that need to be resolved: firstly, the question of how and when to introduce tabular icebergs into the ocean needs to be addressed. For GCM's with active ice shelves, a calving law is needed to decide when to release the tabular iceberg into the ocean. The question of what calving law to use is a topic of ongoing research [Benn et all , 2007; Alley et al , 2008; Levermann et al , 2012; Bassis and Jacobs , 2013] and is still unresolved. One potential way to temporarily bypass this problem would be to run hindcast simulations using historically observed calving events. A related issue is the question of how and when to break the bonds within the freely floating icebergs to simulation iceberg breakup. Without a rule for iceberg breakup, the tabular icebergs would likely drift to unrealistically low latitudes. Finally, further work is needed to understand (and model) the interactions between tabular icebergs and sea ice, and to parametrize the effects of iceberg grounding, as these interactions play a large role in dictating the trajectories of tabular icebergs. None-the-less, the technical framework described in this article is potentially a using step towards including tabular icebergs in global GCM's, and hence a step towards making more accurate projections of future sea level.

## 6 Appendix A

### 6.1 Environmental forces on ice elements

The non-interactive forces on an ice element are as described in [Martin and Adcroft , 2010], and are repeated here for completeness. The forces on an element due to air (a), ocean (o) and sea ice (si) drag are given by

$$(\vec{F}_a) = \rho_a (0.5c_{a,v}WF + c_{a,h}LW)|\vec{u}_a - \vec{u}|(\vec{u}_a - \vec{u}), \quad (11)$$

$$(\vec{F}_o) = \rho_o (0.5c_{o,v}W(D - T_{si})F + c_{o,h}LW)|\vec{u}_o - \vec{u}|(\vec{u}_o - \vec{u}), \quad (12)$$

$$(\vec{F}_{si}) = \rho_{si} (0.5c_{si,v}WT_{si}F + c_{si,h}LW)|\vec{u}_{si} - \vec{u}|(\vec{u}_{si} - \vec{u}). \quad (13)$$

Here  $\rho_a$ ,  $\rho_o$ ,  $\rho_{si}$ , are the density of air, ocean and sea ice, respectively.  $c_{a,v}$ ,  $c_{o,v}$  and  $c_{si,v}$  are the vertical drag coefficients with air, ocean and sea ice, while  $c_{a,h}$ ,  $c_{o,h}$  and  $c_{si,h}$  are the respective horizontal drag coefficients.  $\vec{u}_a$ ,  $\vec{u}_o$ ,  $\vec{u}_{si}$ , are the velocities air, ocean and sea ice, respectively. L, W, T, F and D are the length, width, thickness, free-board and draft of the ice element. The element thickness is related to the draft and free-board by  $T = F + D$  and  $D = \frac{\rho}{\rho_o}T$ , where  $\rho$  is the ice element density.  $T_{si}$  is the sea ice thickness.

518 The wave radiation force ( $\vec{F}_R$ ) is given by

$$\vec{F}_R = \frac{1}{2} \rho_o c_r g a \min(a, F) 2 \frac{WL}{W+L} \frac{\vec{v}_a}{|\vec{v}_a|} \quad (14)$$

519 where  $g$  is the acceleration due to gravity,  $a$  is the wave amplitude empirically related to  
520 the wind speed by  $a = 0.010125|\vec{v}_a - \vec{v}_o|$ , and  $c_{wd}$  is the wave drag coefficient defined as

$$c_{wd} = 0.06 \min\left(\max\left[0, \frac{L - L_c}{L_t - L_c}\right], 1\right), \quad (15)$$

521 where  $L_w = 0.32|\vec{v}_a - \vec{v}_o|^2$  is an empirical wave length,  $L_c = 0.125L_w$  is the cutoff length,  
522 and  $L_t = 0.25L_w$  is the upper limit.

523 The pressure gradient force is approximated as a force due to sea surface slope and  
524 given by

$$\vec{F}_{SS} = -Mg\vec{\nabla}\eta \quad (16)$$

525 where  $\eta$  is the sea surface height.

## 526 6.2 Melt rate parametrization

527 As discussed in Section 2.5, unbounded ice elements in the LBIM decay according  
528 to parameterizations for iceberg decay typically used in iceberg drift models [Martin and  
529 Adcroft , 2010], while ice elements within larger ice structures have only a basal melt  
530 given by the three equation model [Holland and Jenkins , 1999] .

531 For unbonded ice elements, the element thickness decays due to basal melt at a rate  
532  $M_b$ , while the length and width of the elements decay as a result of melt due to wave ero-  
533 sion,  $M_e$ , and melt due to buoyant convection,  $M_v$ . Following Gladstone et al [2001] and  
534 Martin and Adcroft [2010], the basal melt rate, wave erosion melt rate, and buoyant con-  
535 vection melt rate are parameterized by

$$M_b = 0.58|\vec{v} - \vec{v}_0|^{0.8} \frac{\tilde{T}_0 - \tilde{T}}{L^{0.2}} \quad (17)$$

$$M_e = \frac{1}{12} S_s \left(1 + \cos[\pi A_i^3]\right) (\tilde{T}_0 + 2), \quad (18)$$

$$M_v = \left(7.62 \times 10^{-3}\right) \tilde{T}_0 + \left(1.29 \times 10^{-3}\right) \tilde{T}_0^2. \quad (19)$$

536  $\tilde{T}$  is the effective iceberg temperature and is set to  $\tilde{T} = 4^\circ\text{C}$ ,  $\tilde{T}_0$  is the temperature at the  
537 top of the ocean,  $A_i$  is the sea ice area fraction, and  $S_s$  is the sea state, which is given by  
538 the Beaufort scale

$$S_s = \frac{2}{3} |\vec{u}_a - \vec{u}_o|^{\frac{1}{2}} + \frac{1}{10} |\vec{u}_a - \vec{u}_o| \quad (20)$$

541 All three melt rates are in units of meters per day.

542 For elements inside larger structures, the melt due to wave erosion and melt due to  
543 buoyant convection are set to zero, and the basal melt,  $M_s$  is given by the standard three  
544 equation model [Holland and Jenkins , 1999].

## 545 7 Appendix B

### 546 7.1 Modified Verlet Algorithm

547 The LBIM uses a version velocity Verlet time-stepping algorithm, which has been  
548 modified to allow part of the forcing to be calculated implicitly. The traditional velocity  
549 Verlet algorithm is commonly used in molecular dynamics, as it is simple to implement,

second order accurate and computationally efficient [Swope et al , 1982; Omelyan et al , 2002]. Here we modify the traditional scheme to allow for the drag forces to be modeled implicitly, which prevents large accelerations for element's whose mass approaches zero. To do this, we include both an implicit and explicit acceleration,  $a = a^{exp} + a^{imp}$ . The explicit acceleration,  $a^{exp}$  includes all forcing terms which depend only on the previous time step and the current position, while the implicit acceleration,  $a^{imp}$  includes forcing terms which depend on the velocity at the current time step (in particular the drag and Coriolis forces).

Using a time step of  $\Delta t$ , and subscripts to denote the time step (so that  $t_{n+1} = t_n + \Delta t$ ), the modified velocity Verlet scheme can be written as:

$$1) x_{n+1} = x_n + u_n \Delta t + \frac{1}{2} \Delta t^2 \left( a_n^{exp} + a_n^{imp} \right).$$

$$2) \text{Calculate } a_{n+1}^{exp}$$

$$3) \text{Calculate } a_{n+1}^{imp} \text{ and } u_{n+1} = u_n + \frac{\Delta t}{2} \left( a_n^{exp} + a_{n+1}^{exp} \right) + (\Delta t) a_{n+1}^{imp}$$

This scheme reduces to the traditional velocity Verlet when  $a^{imp}$  is set to zero. Note that  $a_{n+1}^{exp} = a_{n+1}^{exp}(x_{n+1}, t_n)$  is an explicit function of  $x_{n+1}$  and other quantities evaluated at time  $t_n$ , while  $a_{n+1}^{imp} = a_{n+1}^{imp}(u_{n+1}, x_{n+1}, t_n)$  additionally depends on  $u_{n+1}$ , and needs to be solved implicitly. For this reason in step three,  $a_{n+1}^{imp}$  and  $u_{n+1}$  need to be solved simultaneously, as described in the next subsection.

In equation (1), the forces due to ocean drag, atmospheric drag and sea ice drag are treated implicitly. The force due to sea surface slope and wave radiation are treated explicitly. The Coriolis term is handled using Crank-Nicolson scheme so that half of the effect is implicit and half is explicit. The elastic part of the interactive forces is treated explicitly, while the interactive damping is handled semi-implicitly in that the drag force on element A by element B depends on the velocities of elements A and B evaluated at time  $t_{n+1}$  and  $t_n$ , respectively.

## 7.2 Solving for the velocity implicitly

Since this modified scheme contains some forcing terms which are handled implicitly,  $a_{n+1}^{imp}$  and  $u_{n+1}$  need to be calculated simultaneously. We demonstrate how this is done, using a simplified one-dimensional version of equation (1), neglecting the atmospheric drag, sea ice drag and Coriolis force, so that the only implicitly treated term is the ocean drag. In this demonstration, we use a superscript to denote the ocean drag force,  $F^o$ , and ocean velocity,  $u^o$ , to avoid confusion with the subscripts indicating time step. We also define an explicit force,  $F^{exp}$ , which accounts for all forces not proportional the element velocity. With these simplifications, the implicit and explicit accelerations are

$$a^{exp} = \frac{1}{M} (\vec{F}^{exp}) \quad (21)$$

$$a^{imp} = \frac{1}{M} (F^o) \quad (22)$$

The ocean drag force at time  $t_{n+1}$  is modeled (mostly) implicitly as

$$F_{n+1}^o = \tilde{c}^o |u_n^o - u_n| (u_n^o - u_{n+1}), \quad (23)$$

where  $\tilde{c}^o$  is the effective drag coefficient, accounting for the dimensions of the ice element (see equation 12).

Step 3 of the modified velocity Verlet scheme can be rewritten by introducing an intermediate velocity  $u^*$ , which only depends on the velocity and acceleration at time  $t_n$ ,

$$u_n^* = u_n + \frac{1}{2} (\Delta t) a_n^{exp}. \quad (24)$$

590 Using this, the updated velocity (Step 3) can be written

$$u_{n+1} = u_n^* + \frac{\Delta t}{2} a_{n+1}^{exp} + (\Delta t) a_{n+1}^{imp}. \quad (25)$$

591 Including the forcing terms into this equations gives

$$u_{n+1} = u_n^* + \frac{\Delta t}{2M} (F_{n+1}^{exp}) + \frac{\Delta t}{M} \left( c_w |u_n^o - u_n| (u_n^o - u_{n+1}) \right) \quad (26)$$

592 Solving for  $u(t_{n+1})$  in terms of quantities which only depend on the previous time step  
593 gives

$$u_{n+1} = \frac{u_n^* + \frac{\Delta t}{2M} (F_{n+1}^{exp}) + \frac{\Delta t}{M} \left( c_w |u_n^o - u_n| (u_n^o) \right)}{\left( 1 + \frac{\Delta t}{M} c_w |u_n^o - u_n| \right)} \quad (27)$$

594 Once the  $u_{n+1}$  has been found, it can be used to calculate the explicit and implicit accelerations,  
595 which are required for the next time step.

596 Finally, we note that the the drag term (equation 23) is not entirely implicit, since  
597 the element velocity inside the absolute value is evaluated at time  $t_n$ , rather than at time  
598  $t_{n+1}$ . This is done so that we can solve for the updated velocity analytically. One conse-  
599 quence of this is that it can give rise to a small oscillation in the element velocity. This  
600 oscillation is addressed by using a predictive corrective scheme: after solving for a first  
601 guess of the velocity at time  $t_{n+1}$ , this estimate of the velocity is used to update the esti-  
602 mate of the drag force (i.e.: inside the absolute value signs). This updated drag, can now  
603 be used to repeat the process described above to find an improved estimate of the velocity.  
604 We found that two iterations were sufficient to remove the unwanted oscillation.

605 The procedure described in this section is easily extended to include more forcing  
606 terms and two dimensions (where it involves inverting a  $2 \times 2$  matrix).

## 607 8 Appendix C

### 608 Connecting bonds across processor boundaries

609 Since the LBIM is parallelized across multiple processors, it often happens that two  
610 elements on different processes are bonded together. Keeping track of numerical bonds  
611 across processor boundaries requires a lot of book keeping. In this section we describe the  
612 how LBIM handles bonds across processor boundaries.

613 The basics of the bond bookkeeping work as follows: consider an element A and  
614 an element B that are bonded together. Each element has a copy of the bond (a piece of  
615 memory which describes the bond between the two elements), which is stored with the  
616 element. Let A-B be the bond stored by element A, and B-A be the bond stored by ele-  
617 ment B. Bond A-B contains a pointer which points to element B and bond B-A contains a  
618 pointer which points to element A.

619 Consider a situation where element A and B are originally on Processor 1, and then  
620 element B moves to Processor 2. When this occurs, the memory assigned to element B  
621 on processor 1 is removed, and is allocated on Processor 2. This means that the pointer  
622 to element B in bond A-B (stored in element A on Processor 1) is no longer assigned.  
623 Similarly, the pointer to element A in bond B-A (stored in element B on Processor 2) is  
624 no longer assigned. Before the next time step, a halo update occurs, so that the there is  
625 a copy of element A in the halo of Processor 2 and a copy of element B in the halo of  
626 Processor 1. After the halo update, the bonds A-B and B-A have to be reconnected on  
627 both Processor 1 and 2. To aid in reconnecting the bonds, a copy of the grid cell number  
628 of element B is stored in the bond A-B and a copy of the grid cell number of element A

629 is stored in the bond B-A. We refer to this as the ‘most recent address’. Before a bond  
630 is moved from one processor to another, the ‘most recent address’ is updated, so that the  
631 bond can be reconnected later. To reconnect bond A-B on Processor 1 (for example), we  
632 find the most recent address of element B, and search through the list of elements in the  
633 grid cell corresponding to the most recent address of element B until element B is found.  
634 The pointer to element B in bond A-B is reassigned, and the bond is said to be connected.

635 The reconnected bond A-B (stored in element A) is said to be working properly  
636 when the following four test pass:

- 637
1. The pointer to element B is assigned on bond A-B.
  2. The corresponding bond B-A exists on element B.
  3. A pointer to element A exists in this bond B-A.
  4. The element A which is being pointed to is the same element A where you started.
- 640

641 A useful tool disconnecting and reconnecting bonds is that each element is assigned a  
642 unique number so that elements are easily identified.

643  
644

**Acknowledgments**

= enter acknowledgments here =

645 **References**

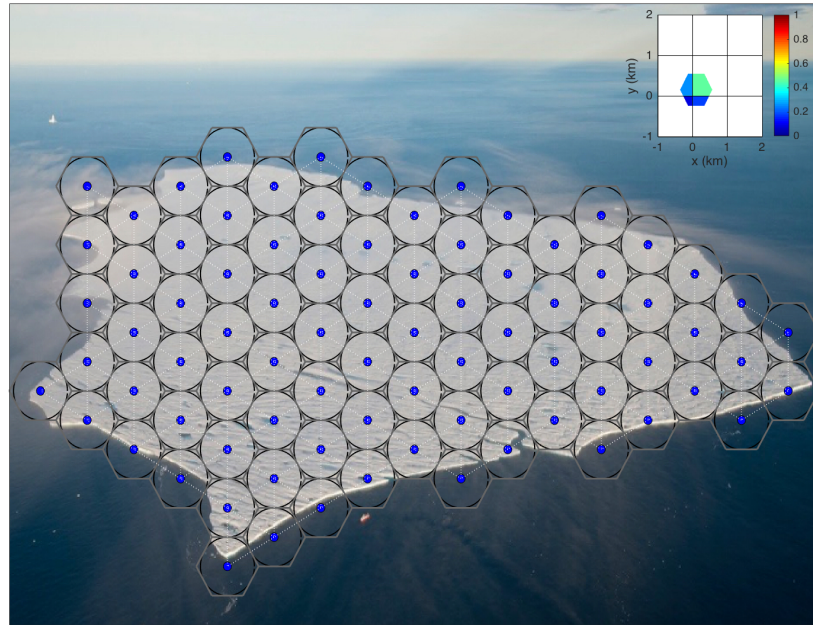
- 646 Asay-Davis, X. S., S. L. Cornford, B. K. Galton-Fenzi, R. M. Gladstone, G. H. Gud-  
 647 mundsson, D. M. Holland, P. R. Holland, and D. F. Martin (2016), Experimental de-  
 648 sign for three interrelated marine ice sheet and ocean model intercomparison projects:  
 649 MISMIP v. 3 (MISMIP+), ISOMIP v. 2 (ISOMIP+) and MISOMIP v. 1 (MISOMIP1).  
 650 *Geoscientific Model Development* 9, no. 7: 2471.
- 651 Arrigo, K. R., G. L. van Dijken, D. G. Ainley, M. A. Fahnestock, and T. Markus (2002).  
 652 Ecological impact of a large Antarctic iceberg. *Geophys. Res. Lett.*, 29(7).
- 653 Alley, R. B., H. J. Horgan, I. Joughin, K. M. Cuffey, T. K. Dupont, B. R. Parizek, S.  
 654 Anandakrishnan, and J. Bassis (2008), A simple law for ice-shelf calving. *Science* 322,  
 655 no. 5906, 1344-1344.
- 656 Bassis, J. N., and S. Jacobs (2013), Diverse calving patterns linked to glacier geometry.  
 657 *Nature Geoscience*, 6(10), 833-836.
- 658 Benn, D. I., C. R. Warren, and R. H. Mottram (2007). Calving processes and the dynam-  
 659 ics of calving glaciers. *Earth-Science Reviews*, 82(3), 143-179.
- 660 Bigg, G. R., Wadley, M. R., Stevens, D. P., and Johnson, J. A. (1997), Modeling the dy-  
 661 namics and thermodynamics of icebergs. *Cold Regions Science and Technology*, 26(2),  
 662 113-135.
- 663 Borstad, C. P., A. Khazendar, E. Larour, M. Morlighem, E. Rignot, M. P. Schodlok, and  
 664 H. Seroussi (2012), A damage mechanics assessment of the Larsen B ice shelf prior to  
 665 collapse: Toward a physically-based calving law, *Geophys. Res. Lett.*, 39, L18502
- 666 Biddle, L. C., J. Kaiser, K. J. Heywood, A. F. Thompson and A. Jenkins (2015), Ocean  
 667 glider observations of iceberg-enhanced biological productivity in the northwestern  
 668 Weddell Sea, *Geophys. Res. Lett.*, 42, 459-465.
- 669 De Rydt, J., and G. H. Gudmundsson (2016), Coupled ice shelf ocean modeling and com-  
 670 plex grounding line retreat from a seabed ridge. *J. of Geophys. Res.: Earth Surface*,  
 671 121(5), 865-880.
- 672 Dunne, J.P., J.G. John,, A.J. Adcroft, S.M. Griffies, R.W. Hallberg, E. Shevliakova, R.J.  
 673 Stouffer, W. Cooke, K.A. Dunne, M.J Harrison, and J.P. Krasting (2012), GFDL's  
 674 ESM2 global coupled climate-carbon Earth System Models. Part I: Physical formula-  
 675 tion and baseline simulation characteristics. *J. of Climate*, 25(19), 6646-6665.
- 676 Depoorter, M. A., J. L. Bamber, J. A. Griggs, J. T. M. Lenaerts, Stefan RM Ligtenberg,  
 677 M. R. van den Broek, and G. Moholdt (2013), Calving fluxes and basal melt rates of  
 678 Antarctic ice shelves. *Nature*, 502(7469), 89-92.
- 679 Determan J., Gerdes R. (1994), Melting and freezing beneath ice shelves: implications  
 680 from a three-dimensional ocean-circulation model. *Ann. Glaciol.*, 20, 413-419.
- 681 Dowdeswell, J. A., and J. L. Bamber (2007), Keel depths of modern Antarctic icebergs  
 682 and implications for sea-floor scouring in the geological record. *Marine Geology*,  
 683 243(1), 120-131.
- 684 Duprat, L. P., G. R. Bigg, and D. J. Wilton (2016), Enhanced Southern Ocean marine pro-  
 685 ductivity due to fertilization by giant icebergs. *Nature Geoscience*.
- 686 Eckert, E. R. G. (1950). Introduction to the Transfer of Heat and Mass. McGraw-Hill.
- 687 Fogwill, C.J., E. van Sebille, E.A. Cougnon, C.S. Turney, S.R. Rintoul, B.K. Galton-Fenzi,  
 688 G.F. Clark, E.M. Marzinelli, E.B. Rainsley, and L. Carter (2016), Brief communication:  
 689 Impacts of a developing polynya off Commonwealth Bay, East Antarctica, triggered by  
 690 grounding of iceberg B09B. *The Cryosphere*, 10(6), p.2603.
- 691 Gladstone, R. M., G. R. Bigg, and K. W. Nicholls. (2001), Iceberg trajectory model-  
 692 ing and meltwater injection in the Southern Ocean (1978-2012). *J. of Geophys. Res.:*  
 693 *Oceans*, 106(C9), 19903-19915.
- 694 Goldberg, D. N., C. M. Little, O. V. Sergienko, A. Gnanadesikan, R. Hallberg, and M.  
 695 Oppenheimer (2012), Investigation of land ice/ocean interaction with a fully coupled  
 696 ice-ocean model: 1. Model description and behavior. *J. of Geophys. Res.: Earth Surface*,  
 697 117(F2).

- 698 Gladish, C. V., D. M. Holland, P. R. Holland, and S. F. Price (2012), Ice-shelf basal chan-  
699 nels in a coupled ice/ocean model. *J. of Glaciol.*, 58(212), 1227-1244.
- 700 Grosfeld K., R. Gerdes, J. Determan (1997), Thermohaline circulation and interaction  
701 between ice shelf cavities and the adjacent open ocean. *J. Phys. Oceanogr.*, **102**, C7,  
702 15959-15610.
- 703 Grosfeld, K., and H. SandhŁger, (2004). The evolution of a coupled ice shelfDocean sys-  
704 tem under different climate states. *Global and Planetary Change*, 42(1), 107-132.
- 705 Hallberg, R., A. Adcroft, J. P. Dunne, J. P., Krasting, R. J., and Stouffer (2013), Sensitiv-  
706 ity of twenty-first-century global-mean steric sea level rise to ocean model formulation.  
707 *J. of Climate*, 26(9), 2947-2956.
- 708 Holland D. M., Jenkins A. (2001), Adaptation of an isopycnic coordinate ocean model for  
709 the study of circulation beneath ice shelves. *Mon. Wea. Rev.*, 129, 1905-1927.
- 710 Holland P. R. and D. L. Feltham (2006), The effects of rotation and ice shelf topography  
711 on frazil-laden Ice Shelf Water plumes. *J. Phys. Oceanogr.*, 36, 2312-2327.
- 712 Holland, D. M., and A. Jenkins (1999), Modeling thermodynamic ice-ocean interactions at  
713 the base of an ice shelf. *J. of Phys. Oceanogr.* 29.8, 1787-1800.
- 714 Hellmer H.H., Olbers D. J. (1989), A two-dimensional model for the thermohaline circula-  
715 tion under an ice shelf. *Antarctic Science*, 1, 325- 336.
- 716 Henderson J., J. S. P. Loe (2016), The Prospects andChallenges for Arctic Oil Develop-  
717 ment. *Oil, Gas and Energy Law Journal (OGEL)*, 14 (2)
- 718 Hopkins, M. A. (1996). On the mesoscale interaction of lead ice and floes. *J. of Geophys.*  
719 *Res.: Oceans*, 101(C8), 18315-18326.
- 720 Gaskill, H. S., and J. Rochester (1984). A new technique for iceberg drift prediction. *Cold*  
721 *Reg. Sci. Technol.*, 8(3), 223-234.
- 722 Jakobsen, T. (2001). Advanced character physics. *In Game Developers Conference*, Vol. 3.
- 723 Jenkins, A., P. Dutrieux, S. S. Jacobs, S. D. McPhail, J. R. Perrett, A. T. Webb, and D.  
724 White (2010), Observations beneath Pine Island Glacier in West Antarctica and implica-  
725 tions for its retreat. *it Nature Geo.*, 3(7), 468-472.
- 726 Jacobs, S. S., A. Jenkins, C. F. Giulivi, and P. Dutrieux (2011). Stronger ocean circulation  
727 and increased melting under Pine Island Glacier ice shelf. *Nature Geo.*, 4(8), 519-523.
- 728 Jongma, J. I., E. Driesschaert, T. Fichefet, H. Goosse, and H. Renssen (2009), The ef-  
729 fect of dynamic-thermodynamic icebergs on the Southern Ocean climate in a three-  
730 dimensional model, *Ocean Modell.*, 26, 104Ð113.
- 731 Kubat I., M. Sayed, S. Savage, T. Carrières (2005), An operational model of iceberg drift  
732 *Int. J. Off. Polar Eng.*, 15 (2), 125Ð131
- 733 Lewis E.L. and R.G. Perkin (1986), Ice pumps and their rates. *J. of Geophys. Res.*, 91,  
734 11756-11762.
- 735 Losch, M. (2008). Modeling ice shelf cavities in a z coordinate ocean general circulation  
736 model. *J. of Geophys. Res.: Oceans*, 113(C8).
- 737 Li, B., H. Li, Y. Liu, A. Wang and S. Ji (2014), A modified discrete element model for  
738 sea ice dynamics. *Acta Oceanologica Sinica*, 33(1), 56-63.
- 739 Liu, M. B. and G. R. Liu (2010), Smoothed particle hydrodynamics (SPH): an overview  
740 and recent developments. *Archives of computational methods in engineering*, 17(1), 25-  
741 76.
- 742 Lichéy, C., and H. H. Hellmer (2001). Modeling giant-iceberg drift under the influence of  
743 sea ice in the Weddell Sea, Antarctica. *J. of Glaciol.*, 47(158), 452-460.
- 744 Levermann, A., T. Albrecht, R. Winkelmann, M. A. Martin, M. Haseloff, and I. Joughin.  
745 (2012), Kinematic first-order calving law implies potential for abrupt ice-shelf retreat.  
746 *The Cryosphere*, 6(2), 273-286.
- 747 Mountain, D. G. (1980). On predicting iceberg drift. *Cold Reg. Sci. Technol.*, 1(3-4), 273-  
748 282.
- 749 Martin, T., and Adcroft, A. (2010), Parameterizing the fresh-water flux from land ice to  
750 ocean with interactive icebergs in a coupled climate model. *Ocean Modelling*, 34(3),

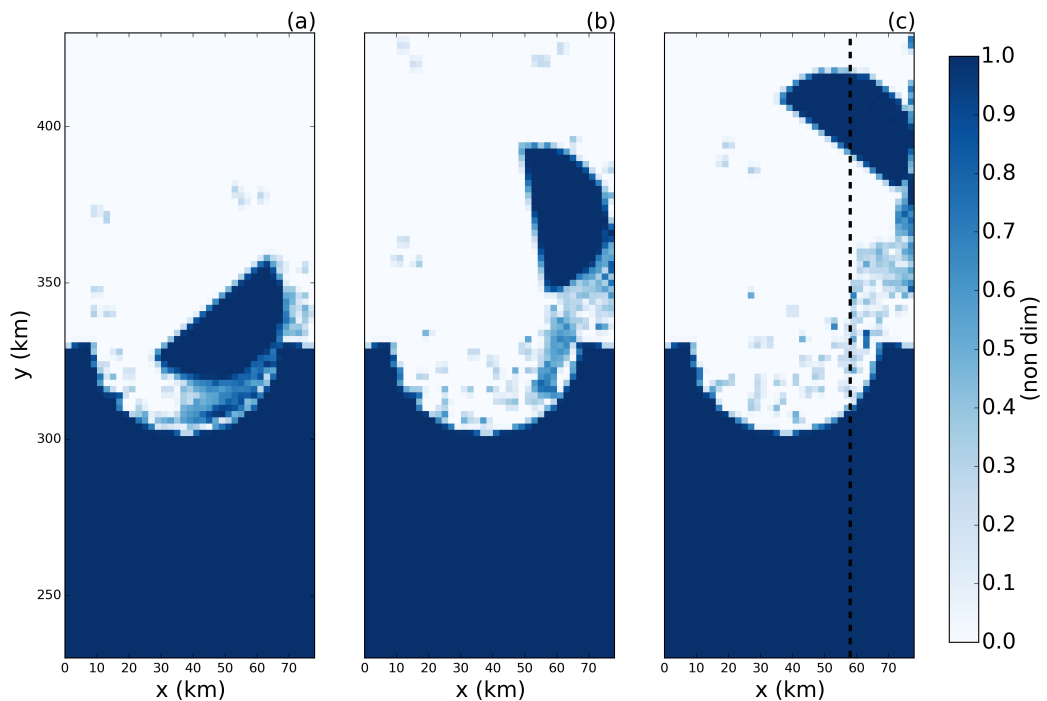
- 751                  111-124.
- 752 Marsh, R., V. O. Ivchenko, N. Skliris, S. Alderson, G. R. Bigg, G. Madec, A. T. Blaker  
 753                  Y. Aksenov, B. Sinha, A.C. Coward, and J.L. Sommer (2015), NEMO $\delta$ ICB (v1. 0):  
 754                  interactive icebergs in the NEMO ocean model globally configured at eddy-permitting  
 755                  resolution. *Geoscientific Model Development* 8, no. 5 (2015): 1547-1562.
- 756 MacAyeal D.R. (1984), Thermohaline Circulation Below the Ross Ice Shelf: A Conse-  
 757                  quence of Tidally Induced Vertical Mixing and Basal Melting. *J. Geophys. Res.*, 89,  
 758                  597-606
- 759 Merino, N., Le Sommer, J., Durand, G., Jourdain, N. C., Madec, G., Mathiot, P., and  
 760                  Tournadre, J. (2016), Antarctic icebergs melt over the Southern Ocean: climatology and  
 761                  impact on sea ice. *Ocean Modelling*, 104, 99-110.
- 762 Nicholls K.W. (1996), Temperature variability beneath Ronne Ice Shelf, Antarctica, from  
 763                  thermistor cables. *J. Phys. Oceanogr.*, 11, 1199-1210.
- 764 Nicholls KW, Østerhus S, Makinson K (2009), Ice-Ocean processes over the continental  
 765                  shelf of the southern Weddell Sea, Antarctica: a review. *Rev. Geophys.* 47(3).
- 766 Omelyan, I. P., M. I. Mryglod, and R. Folk (2002), Optimized Verlet-like algorithms for  
 767                  molecular dynamics simulations. *Physical Review E*, 65(5), 056706.
- 768 Rignot, E., S. Jacobs, J. Mouginot, and B. Scheuchl (2013), Ice-shelf melting around  
 769                  Antarctica. *Science*, 341, no. 6143 (2013): 266-270.
- 770 Robinson, N. J., M. J. M. Williams, P. J. Barrett, and A. R. Pyne (2010), Observations of  
 771                  flow and ice-ocean interaction beneath the McMurdo Ice Shelf, Antarctica, *J. Geophys.*  
 772                  *Res.*, 115, C03025
- 773 Pizzolato, L., S. E. Howell, C. Derksen, J. Dawson, L. Copland (2014), Changing sea ice  
 774                  conditions and marine transportation activity in Canadian Arctic waters between 1990  
 775                  and 2012, *Climatic Change* 123 (2), 161173.
- 776 Pan, W., A. M. Tartakovsky, and J. J. Monaghan (2013). Smoothed particle hydrodynam-  
 777                  ics non-Newtonian model for ice-sheet and ice-shelf dynamics. *J. of Comp. Phys.*, 242,  
 778                  828-842.
- 779 Pralong, A., and M. Funk (2005), Dynamic damage model of crevasse opening and appli-  
 780                  cation to glacier calving, *J. Geophys. Res.*, 110, B01309.
- 781 Sergienko, O. V. (2013). Basal channels on ice shelves. *J. of Geophys. Res.: Earth Surface*,  
 782                  118(3), 1342-1355.
- 783 Silva, T. A. M., Bigg, G. R., and Nicholls, K. W. (2006), Contribution of giant icebergs to  
 784                  the Southern Ocean freshwater flux. *J. of Geophys. Res.: Oceans*, 111(C3).
- 785 Smith, K., B. Robison, J. Helly, R. Kaufmann, H. Ruhl, H., T. Shaw, and M. Vernet  
 786                  (2007), Free-drifting icebergs: Hotspots of chemical and biological enrichment in the  
 787                  Weddell Sea, *Science*, 317, 478-482.
- 788 Shepherd, A., and D. Wingham (2007). Recent sea-level contributions of the Antarctic and  
 789                  Greenland ice sheets. *Science*, 315(5818), 1529-1532.
- 790 Stern, A. A., D. M. Holland, P. R. Holland, A. Jenkins and J. Sommeria (2014), The ef-  
 791                  fect of geometry on ice shelf ocean cavity ventilation: a laboratory experiment. *Experi-*  
 792                  *ments in Fluids*, 55(5), 1-19.
- 793 Stern, A.A., Johnson, E., Holland, D.M., Wagner, T.J., Wadhams, P., Bates, R., Abraham-  
 794                  sen, E.P., Nicholls, K.W., Crawford, A., Gagnon, J. and Tremblay, J.E. (2015), Wind-  
 795                  driven upwelling around grounded tabular icebergs. *J. of Geophys. Res.: Oceans*, 120(8),  
 796                  5820-5835.
- 797 Stern, A. A., A. Adcroft, and O. Sergienko (2016), The effects of Antarctic iceberg calv-  
 798                  ing size distribution in a global climate model. *J. of Geophys. Res.: Oceans*, 121(8),  
 799                  5773-5788.
- 800 Swope, W. C., H. C. Andersen, P. H. Berens, and K. R. Wilson (1982), A computer sim-  
 801                  ulation method for the calculation of equilibrium constants for the formation of physi-  
 802                  cal clusters of molecules: Application to small water clusters. *The Journal of Chemical*  
 803                  *Physics* 76, no. 1, 637-649.

- 804 Tournadre, J., N. Bouhier, F. Girard-Ardhuin, and F. RÖmy (2016), Antarctic icebergs dis-  
805 tributions 1992-2014. *J. Geophys Res: Oceans*.
- 806 Turnbull I.D., N. Fournier, M. Stolwijk, T. Fosnaes, D. McGonigal (2015), Operational  
807 iceberg drift forecasting in Northwest Greenland, *Cold Reg. Sci. Technol.* 110, 1-18
- 808 Unger, J. D., 2014. Regulating the Arctic Gold Rush: Recommended Regulatory Reforms  
809 to Protect Alaska's Arctic Environment from Offshore Oil Drilling Pollution . *Alaska L.*  
810 *Rev*, 31
- 811 Vernet, M., et al. (2012), Islands of ice: Influence of free-drifting Antarctic icebergs on  
812 pelagic marine ecosystems, *Oceanography*, 25(3), 38Ð39
- 813 Wagner, T. J., Wadhams, P., Bates, R., Elosegui, P., Stern, A., Vella, D., E. P. Abraham-  
814 sen, A. Crawford, and Nicholls, K. W. (2014), The ÒfootlooseÓ mechanism: Iceberg  
815 decay from hydrostatic stresses. *Geophys. Res. Lett.*, 41(15), 5522-5529.
- 816 Weeks, W. F., and W. J. Campbell (1973). Icebergs as a fresh-water source: an appraisal.  
817 *J. of Glaciol.*, 12(65), 207-233.
- 818 White, L., A. Adcroft, and R. Hallberg (2009), High-order regridding-remapping schemes  
819 for continuous isopycnal and generalized coordinates in ocean models. *J. of Comp.*  
820 *Phys.*, 228(23), 8665-8692.

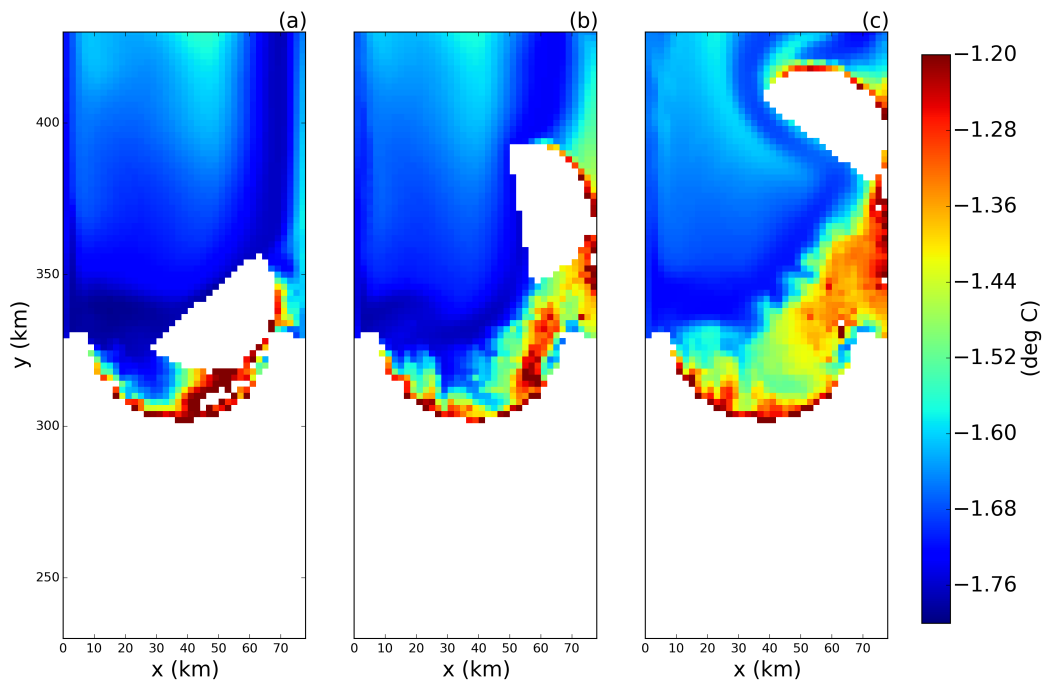
Parameter	Symbol	Value	Unit
Domain Length	$L_x$	80	km
Domain Width	$L_y$	480	km
Horizontal Resolution	$\Delta x$	2	km
Number of vertical layers	$N_l$	72	non-dim
Horizontal Viscosity	$\nu_H$	6.0	$\frac{m^2}{s}$
Diapycnal Viscosity	$\nu_V$	$10^{-3}$	$\frac{m}{s}$
Horizontal Diffusivity	$\epsilon_H$	1.0	$\frac{m^2}{s}$
Diapycnal Diffusivity	$\epsilon_V$	$5 \times 10^{-5}$	$\frac{m^2}{s}$
Initial Surface Temperature	$T_t$	-1.9	°C
Initial Bottom Temperature	$T_b$	1.0	°C
Initial Surface Salinity	$S_t$	33.8	psu
Initial Bottom Salinity	$S_b$	34.7	psu
Maximum Ocean depth	$H_{ocean}$	720	m
Relaxation Time of Sponge Layer	$T_{sponge}$	0.1	days
Time Step for Static Shelf Experiment	$dt_{Static}$	1000	s
Time Step for Iceberg Calving Experiment	$dt_{Calving}$	10	s



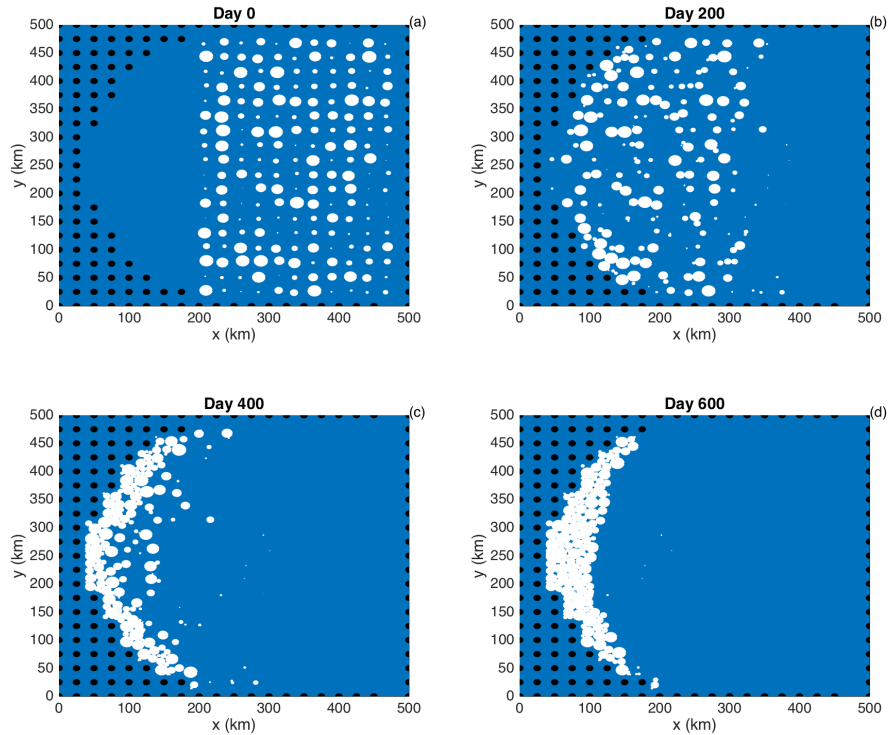
821 **Figure 1.** Schematic showing how Lagrangian elements are used when modeling tabular icebergs. La-  
 822 grangian elements (blue dots) are initialized in a staggered lattice covering the surface area of the iceberg.  
 823 For purposes of mass aggregation, the ice elements are assumed to have hexagonal shape (grey hexagons).  
 824 For purposes of element interactions, the ice elements are assumed to be circular (black circles). Elements  
 825 are initially bonded to adjacent elements using numerical bonds (dashed white lines). These numerical bonds  
 826 form equilateral triangles which give the shape rigidity. The inset panel shows a schematic of the intersection  
 827 of a hexagonal element and the ocean grid. The colors indicate the fraction of the hexagon that lies in each  
 828 grid cell. These fractions are used as weights to spread LBIM properties to the ocean grid (see text for more  
 829 details) The background photo in the larger schematic is an areal photograph of iceberg PIIB (Area= 42 km<sup>2</sup>)  
 830 taken in Baffin Bay in 2012. The red ship can be identified on the bottom of the photo for scale.



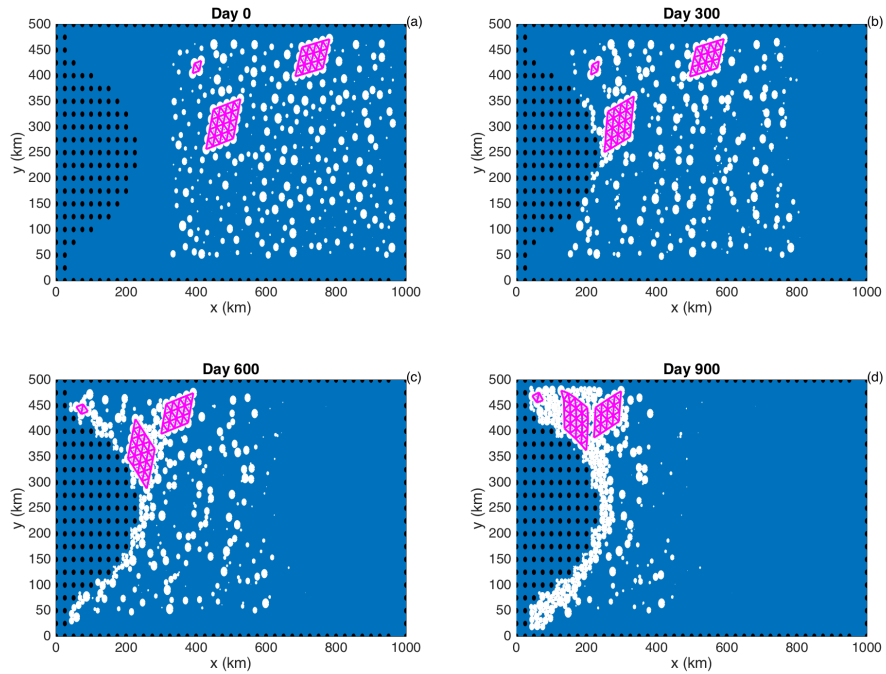
831 **Figure 2.** Snapshots of the fraction of ice cover in the LBIM tabular iceberg calving simulation. Snapshots  
832 are taken (a) 7, (b) 15, and (c) 30 days after calving. The dashed line in panel (c) shows the location of the  
833 vertical transects shown in Figures 7 and 8.



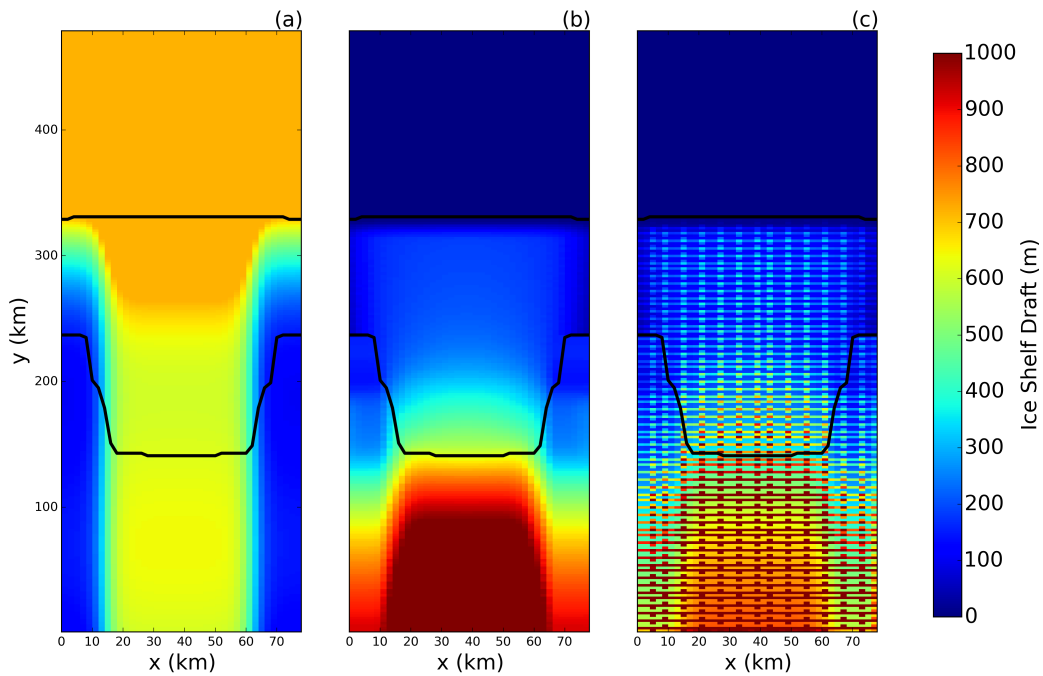
834 **Figure 3.** Snapshots of the sea surface temperature in the LBIM tabular iceberg calving simulation. Snap-  
835 shots are taken (a) 7, (b) 15, and (c) 30 days after calving. Regions with ice area fraction = 1 area plotted in  
836 white.



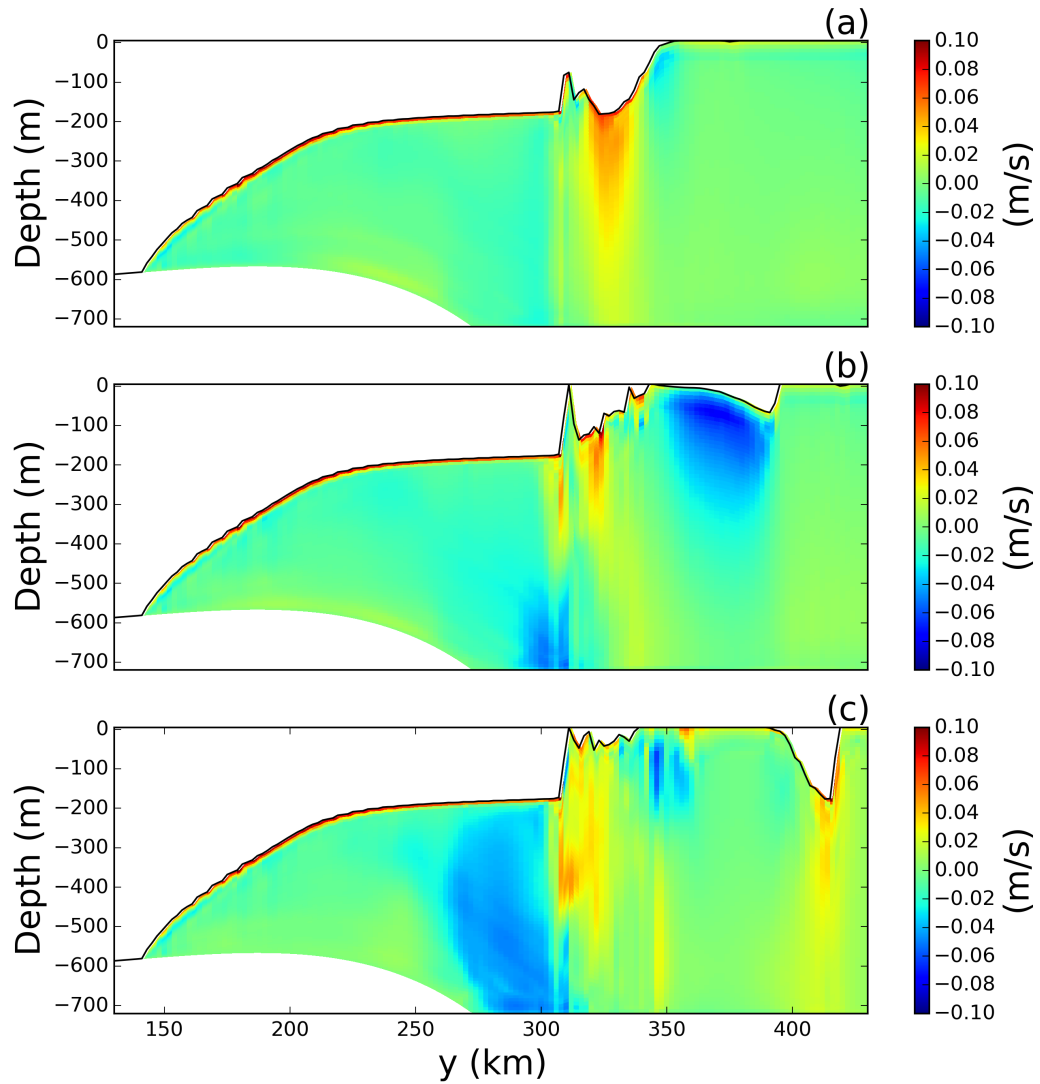
837 **Figure 4.** Results of an ice-only LBIM simulation with no bonds between ice elements. Ice elements are  
 838 initialized throughout the domain, as shown in panel (a). The elements are forced by an imposed westward  
 839 ocean current of  $u=0.1\text{m/s}$  (no ocean model is used). Forces due to sea surface slope, atmospheric drag, Cori-  
 840 olis and sea ice drag are set to zero. The figure shows snapshots of ice element positions at time (a)  $t=0$ , (b)  
 841 200, (c) 400, (d) 600 days. The size of the dots shows the surface area (and interaction diameter) of each ice  
 842 element. Land points are shown by black circles.



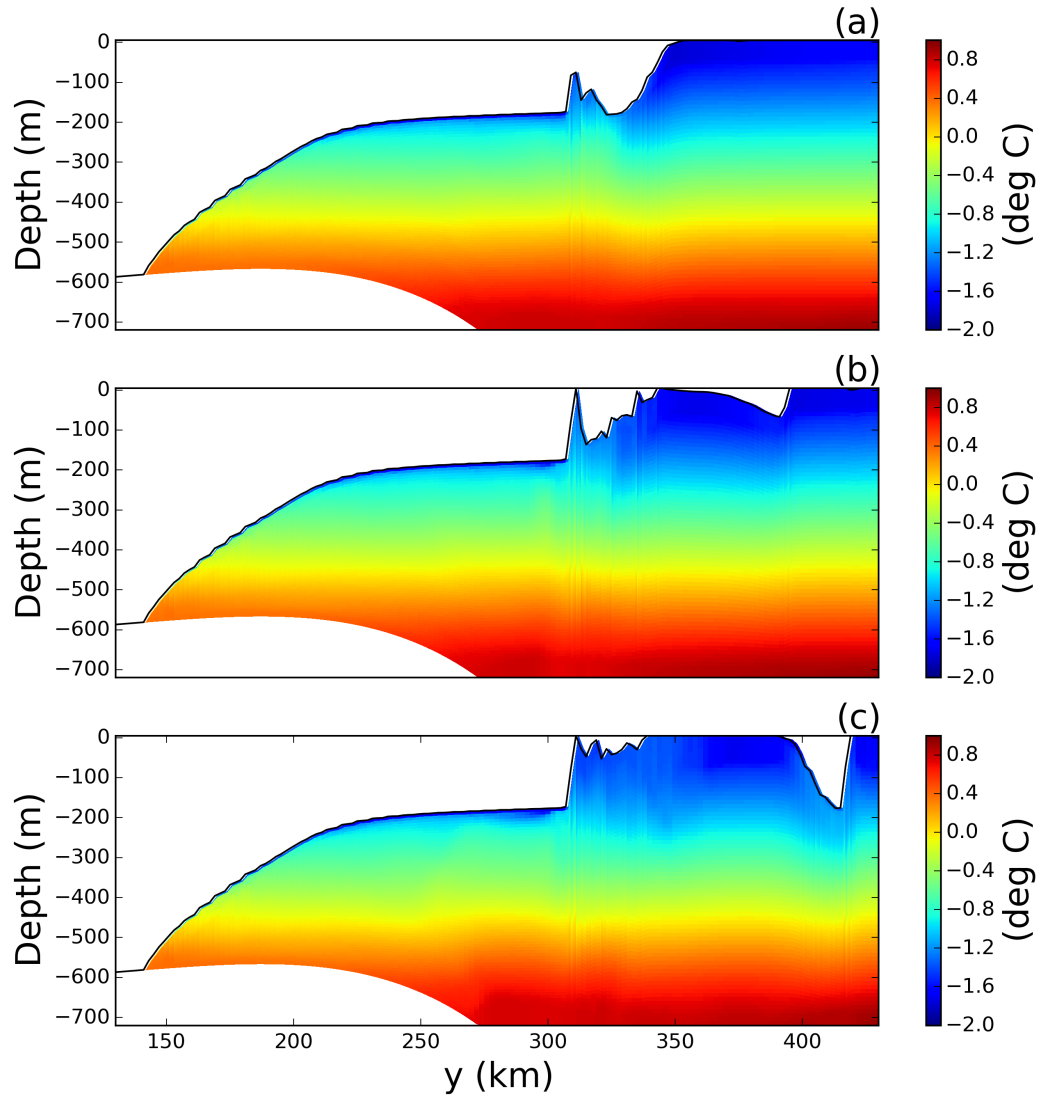
843 **Figure 5.** Results of an ice-only LBIM simulation using bonds between elements. Ice elements are ini-  
 844 tialized throughout the domain, as shown in panel (a). Three tabular icebergs are included, with 25, 16 and 4  
 845 elements respectively. The elements are forced by an imposed westward ocean current of  $u=0.1\text{m/s}$  (no ocean  
 846 model is used). Forces due to sea surface slope, atmospheric drag, Coriolis and sea ice drag are set to zero.  
 847 The figure shows snapshots of ice element positions at time (a)  $t=0$ , (b) 300, (c) 600, (d) 900 days. The size  
 848 of the dots shows the surface area (and interaction diameter) of each ice element. Bonds between ice elements  
 849 are plotted in magenta. Land points are shown by black circles.



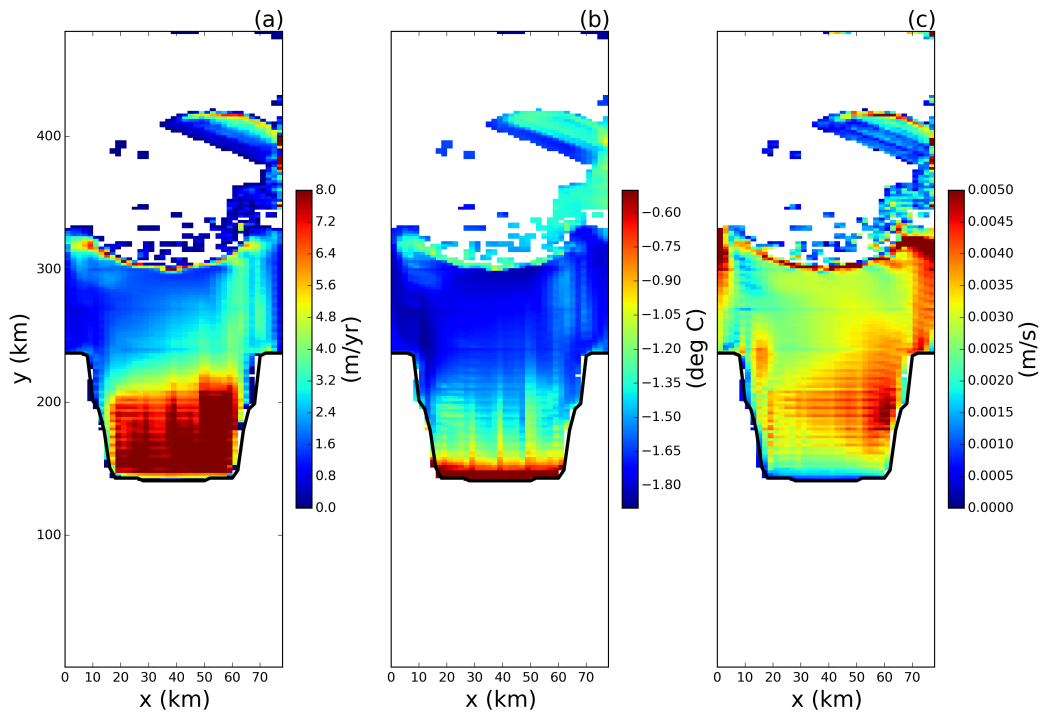
850      **Figure 6.** (a) Ocean bottom topography and (b) ice-shelf draft used to initialize the tabular iceberg calving  
 851      simulation. The ice draft is calculated from the total mass in an ocean grid cell after the mass-spreading  
 852      interpolation has been applied (as explained in Section 2.3). (c) Initial ice draft that would be calculated if the  
 853      mass-spreading interpolation were not used (i.e.: elements treated as point masses).



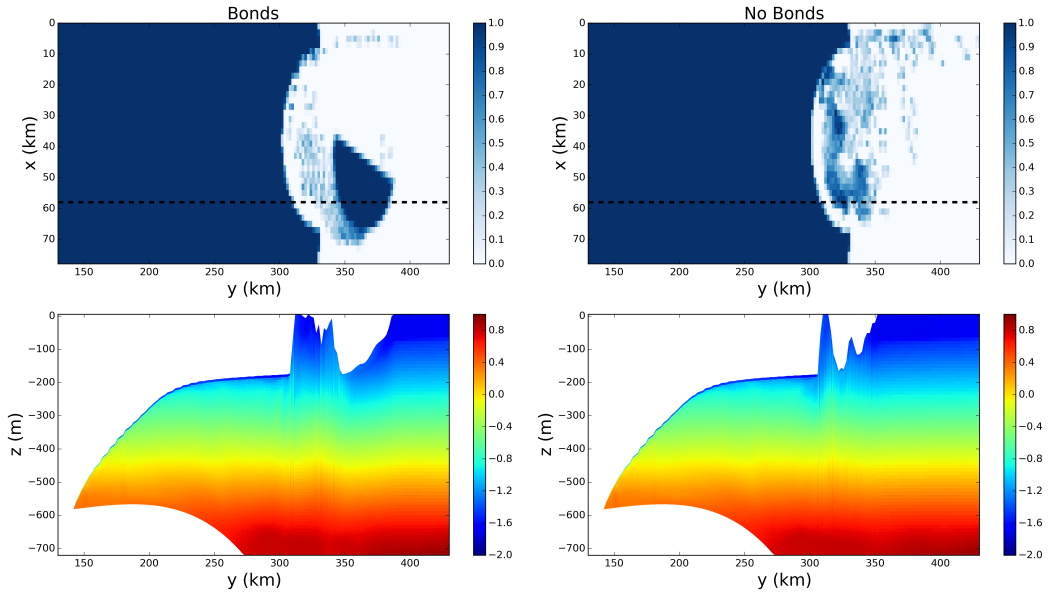
854 **Figure 7.** Snapshots of vertical sections of meridional velocity at  $x = 58$  km in the LBIM tabular ice-  
 855 berg calving simulation. Snapshots are taken (a) 7, (b) 15, and (c) 30 days after calving. The position of the  
 856 transects is shown by the dashed line in Figure 2c.



857 **Figure 8.** Snapshots of vertical sections of ocean temperature at  $x = 58$  km in the LBIM tabular iceberg  
858 calving experiment. Snapshots are taken (a) 7, (b) 15, and (c) 30 days after calving. The position of the  
859 vertical transects is shown by the dashed lines in Figure 2c.



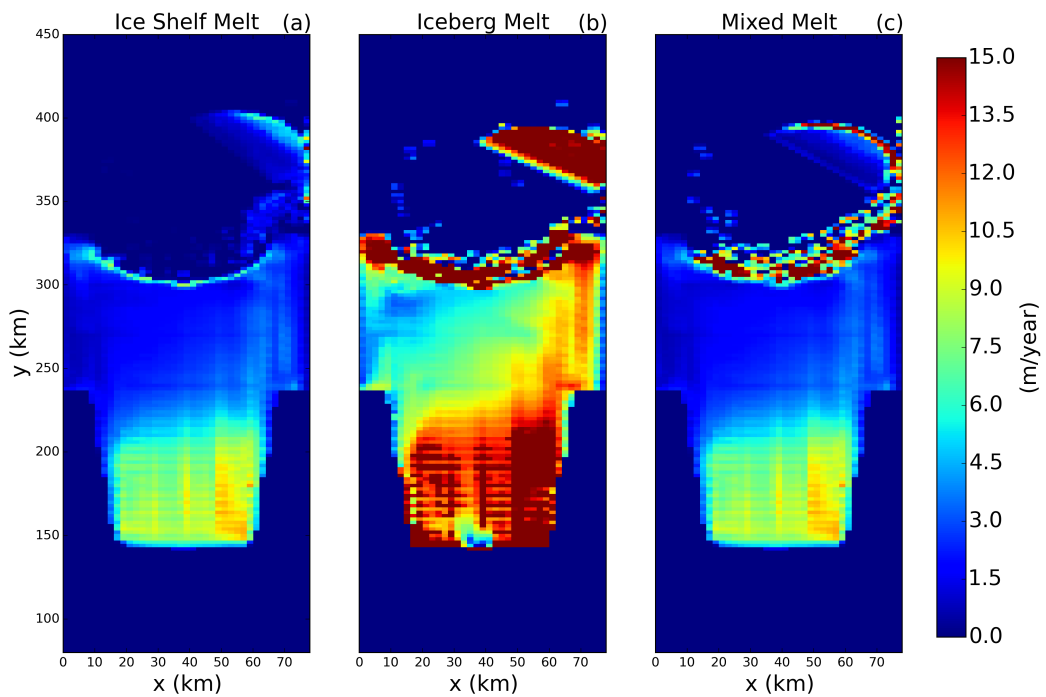
860 **Figure 9.** Results of the tabular iceberg calving simulation 30 days after the iceberg calves. The three panels  
861 show snapshots of the (a) melt rate, (b) top-of-ocean temperature and (c)  $u^*$  at the base of the ice shelf.  
862 Fields are only shown in regions where the ice area fraction is  $\geq 0.8$ .



863 **Figure 10.** Results from the tabular iceberg calving experiment with and without iceberg bonds. The top  
 864 row shows the fractional ice cover for the simulations (a) with and (b) without numerical bonds. The bottom  
 865 row shows the corresponding vertical temperature section at  $x = 58$  km for the simulation (c) with and (d)  
 866 without bonds. The location of the vertical transects in panels (c) and (d) are shown by the dashed lines in  
 867 panels (a) and (b), respectively. All snapshots are taken at time  $t = 30$  days. The simulations use wind stress  
 868  $\vec{\tau} = <0.0, 0.05>$ .

869

**9 Extra Figure:**



870 **Figure 11.** Melt rate 30 days after calving for simulations using (a) three equation  
871 model, (b) icebergs drift parametrization, (c) a mixture between the two (as described in Section 2.5.)

872      **10 Supplementary Material**

873      The experiment configuration used to initialize the calving tabular iceberg simulation  
874      (in this study) is the same as that of the Ocean0 setup in the MISOMIP, with the follow-  
875      ing three changes made:

- 876      1. The ‘calving criteria’ used in the MISOMIP study (which states that all points in  
877      the ice shelf with thickness less than 100m are set to zero thickness) has not been  
878      used.
- 879      2. The ice shelf has been thickened on the flanks of the domain, so that the latitude of  
880      the grounding line increases away from the center of the ice shelf.
- 881      3. The ice shelf is configured to be symmetric about its meridional center line ( $x =$   
882       $\frac{L_x}{2}$ ). This was achieved by using the average of the left and right flanks of the ice-  
883      shelf thickness.

884      These three changes were made in order to make the circulation beneath the ice shelf eas-  
885      ier to interpret.